## Supplementary Information

## Ni$_x$:V$_y$–Se Nanoparticle Decorated Hierarchical Porous Zn–Co–P Nanowire Arrays Electrode For High Energy Density Asymmetric Supercapacitors

JiuYi Dai[a], Soram Bobby Singh[a], Bollu Manoj[a], Nam Hoon Kim*[a,] and Joong Hee Lee*[a,b]

*[a]Department of Nano Convergence Engineering, Jeonbuk National University, Jeonju, Jeonbuk, 54896, Republic of Korea. E-mail:jhl@jbnu.ac.kr (Joong Hee Lee)*

*[b]Carbon Composite Research Centre, Department of Polymer-Nano Science and Technology, Jeonbuk National University, Jeonju, Jeonbuk 54896, Republic of Korea.*

*\*Corresponding authors:*

Email address: jhl@jbnu.ac.kr (Prof. Joong Hee Lee)

nhk@jbnu.ac.kr (Nam Hoon Kim)

**Synthesis of the $Fe_2O_3$@CNF/N-rGO**

$Fe_2O_3$@CNF/N-rGO aerogel was prepared as represented in the scheme. Here, the carbon nanofiber (CNF) was prepared thorough a two-step process. Firstly, the polyacrylonitrile (PAN) polymer nanofiber (NFs) paper precursor was fabricated from the PAN/DMF solution by the electrospinning process. The PAN NFs paper was then cut into pieces and dispersed into DI water. To obtain a homogeneously dispersed PAN NFs gel solution a tip-sonicator was used for 1 h. The PAN NFs aerogel was then obtained by frozen in liquid nitrogen followed by the freeze-drying process. Finally, the CNF was fabricated from PAN NFs aerogel through two-step thermal annealing process say stabilization and carbonization processes, similar to our previous work [1]

Graphene oxide was prepared by the chemical oxidation of the graphite powder following the well-known Hummer's method, as reported in our earlier study.

Synthesis of 3D $Fe_2O_3$ NP@CNF/N-rGO composite was carried out as follows: 50 mg GO powder and 50 mg of as-prepared CNFs were separately dispersed into 10 mL of DI water with ultrasonication for 2 h. Then, two separate solutions of GO and CNFs was mixed together with continuous stirring for 30 min. The iron precursor solution (0.5mmol $FeCl_3 \cdot 6H_2O$ in 5 mL DI water) and 2 ml $NH_3 \cdot H_2O$ (28%) were then added dropwise into the above mixed solution under vigorous stirring for 1h at room temperature. Subsequently, the iron precursor contained mixed solution was transferred into a 50 mL Teflon-lined stainless-steel autoclave. The autoclave was sealed, maintained at 180 °C for 12 h, and then slowly cooled down to the room temperature naturally to obtain a black cylinder hydrogel. The black cylinder hydrogel was carefully fetched out and put into DI water to dialyze for 12 h. Finally, the dried $Fe_2O_3$@CNF/N-rGO cylinder aerogel was obtained by freeze-drying. For comparison, $Fe_2O_3$ NP@PAN NF/N-rGO was prepared using the same procedure.

**Fabrication of solid-state asymmetric supercapacitors:**

The electrochemical performance of all-solid-state ASC was measured under a two-electrode system. In the two-electrode system, $Ni_{0.5}V_{0.5}$–Se/Zn-Co-P NWAs grown 3D porous Ni foam was used as the positive electrode, $Fe_2O_3$@CNFs/N-rGO coated on Ni foam as the negative electrode and KOH/PVA solid-gel as solid-state electrolyte as well as separator. The KOH/PVA gel electrolyte was prepared using the following procedure: 2 g KOH and 2 g PVA (Mw = 98000) were dissolved in 22 mL DI water and then heated at 95 °C for 2 h under vigorous stirring. The electrodes and separator were soaked in the electrolyte for 10 min. and then allowed to solidify the sample by freeze and unfreeze repeatedly. To realize a high electrochemical property we optimized the mass ratio of the $Ni_{0.5}V_{0.5}$–Se/Zn-Co-P NWAs to $Fe_2O_3$@CNFs/N-rGO around~ 0.43 and the working voltage window of

the device to ~ 1.7 V. The optimal mass ratio of positive materials to negative materials was counted by Equation (5).

**Materials characterization**

The field-emission scanning electron microscope (FE-SEM; SUPRA 40 VP; Carl Zeiss, Germany) was used to characterize the surface morphology of the as-synthesized materials. The EDAX analysis (SUPRA 40 VP; Carl Zeiss, Germany) was used to investigate the quantity of the elemental composition of the as-obtained materials. The transmission electron microscopy (TEM) and high-resolution TEM (HR-TEM; H-7650; Hitachi Ltd., Japan) were used to examine the intrinsic morphology of the as-synthesized electrode material. The STEM-energy dispersive X-ray spectroscopy (EDS) mapping was used to analyze the elemental distribution of the as-obtained electrode materials. We examined the crystallinity of the as-synthesized materials by X-ray diffraction (XRD) (Rigaku Corporation, Japan, Cu Kα radiation ($\lambda$ = 0.154 nm)). The theta probe AR-XPS system (Thermo Fisher Scientific, UK) was used to investigate the elemental compositions and valence states of the as-obtained electrode material. The $N_2$ sorption isotherms analysis was used to measure the SSA and the pore-size distribution of the as-obtained electrode material (at 77K; Micromeritics ASAP 2020).

**Electrochemical measurement**

The electrochemical workstation (CHI660D, CH Instruments, Inc., USA) was used to study the electrochemical properties of materials under a three-electrode configuration system. The aqueous 2 M KOH solution was used as the electrolyte. In a three-electrode configuration system, the Pt foil was used as counter electrodes, the Ag/AgCl/3.0 mol/kg KCl was used as the reference electrode, and the as-obtained pristine Zn-Co-P, Ni–Se/Zn-Co-P, V–Se/Zn-Co-P, $Ni_{0.5}V_{0.5}$–Se/Zn-Co-P, $Ni_{0.25}V_{0.75}$–Se/Zn-Co-P, and $Ni_{0.75}V_{0.25}$–Se/Zn-Co-P, electrodes were directly used as the working electrode. The mass loading for the Zn-Co-P, Ni–Se/Zn-Co-P, V–Se/Zn-Co-P, $Ni_{0.5}V_{0.5}$–Se/Zn-Co-P, $Ni_{0.25}V_{0.75}$–Se/Zn-Co-P, and $Ni_{0.75}V_{0.25}$–Se/Zn-Co-P are 2.2 mg cm$^{-2}$, 2.4 mg cm$^{-2}$, 2.4 mg cm$^{-2}$, 2.5 mg cm$^{-2}$,2.4 mg cm$^{-2}$, and 2.5mg cm$^{-2}$, respectively. The electrochemical impedance spectroscopy (EIS) test was examined by using a 5 mV amplitude with a frequency range from 0.01 Hz to 100 kHz.

**Calculations**

The areal capacity ($C_{ac}$, mAh cm$^{-2}$) and the specific capacity ($C_{sc}$, mAh g$^{-1}$) of the as-obtained materials under the three-electrode configuration system and the ASC device were counted from general charge and discharge (GCD) curves using the following Equations Eqs.S (1) and Eqs.S (2) [2-6]:

$$C_{ac} = \frac{2I \times \int Vdt}{AV} \tag{1}$$

$$C_{sc} = \frac{2I \times \int Vdt}{mV} \tag{2}$$

Where the "I" (mA) is the current of the system during the discharge process, the "A" ($cm^{-2}$) is the area of the active electrode, the "m" (g) is the mass of the active electrode material, and the "∫Vdt" is the absolutely integral area of the GCD curve (discharge process). The energy densities (E, W h $kg^{-1}$) and the power densities (P, W $kg^{-1}$) of the assembled ASC device were calculated using the following Equations Eqs.S (3) and Eqs.S (4)[2-6]:

$$E = \frac{I \times \int Vdt}{m \times 3.6} \tag{3}$$

$$P = \frac{E}{t} \times 3600 \tag{4}$$

Where the "I" (mA) is the current of the ASC device, the "∫Vdt" is the absolutely integral area of the GCD curve (discharge part), the "m" (g) is the mass of the material (active electrode), and "t" is the discharge time. The mass ratio of the $Ni_{0.5}V_{0.5}$–Se/Zn-Co-P (positive) and $Fe_2O_3$@CNFs/N-rGO (negative) materials were counted by Equation Eqs.S(5)[2-6]:

$$\frac{m_+}{m_-} = \frac{C_- \times V_-}{C_+ \times V_+} \tag{5}$$

where the "m−" is the negative materials mass, the "m+" is the positive materials mass; the "C−" is the specific capacity (negative materials), the "C+" is the specific capacity (positive materials); and "V" is the working voltage widow for the negative (-) and positive (+) materials.
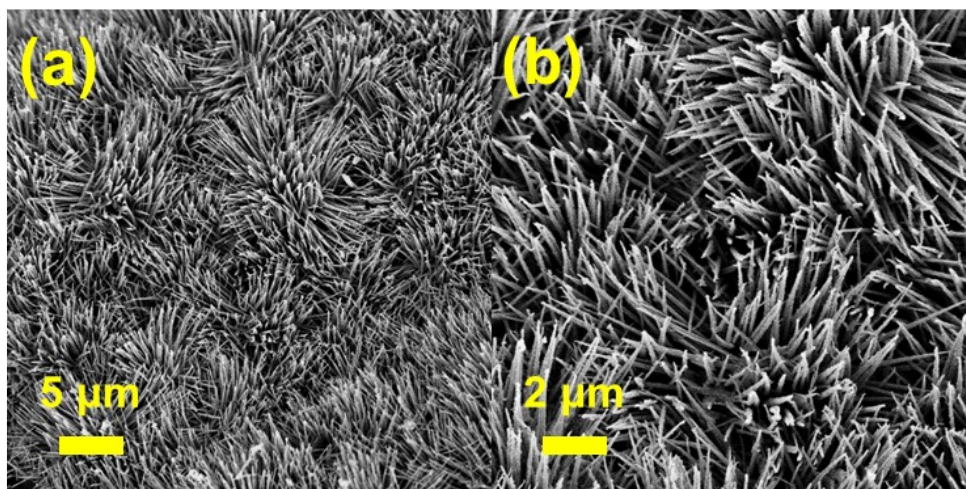
**Fig. S1** FE-SEM image of as-synthesized (a-b) Zn-Co precursor
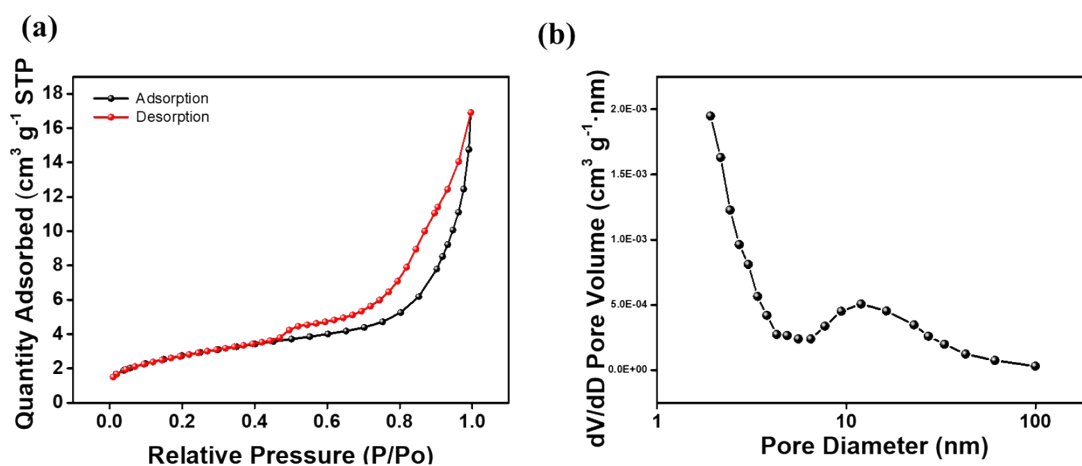
**Fig. S2** (a) and (b) show the adsorption-desorption isotherms and pore size distribution of Zn–Co–P NWAs electrode.

The isotherms depict a type IV hysteresis loop, typical of mesoporous materials, Fig S2a. This further confirms the presence of mesopores in our material. The steep uptake at high relative pressures (P/P$_o$ close to 1) suggests the presence of larger mesopores or macropores, which can enhance electrolyte diffusion and improve the overall electrochemical performance. The measured BET surface area of 9.9623 m²/g indicates a significant amount of surface area available for electrochemical reactions. Although this value might not seem extremely high, the presence of well-distributed pores can significantly enhance electrochemical performance. The pore size distribution, Fig. S2b shows a high concentration of pores in the mesoporous range (2-50 nm). The presence of mesopores is beneficial for electrochemical applications as they provide a balance between surface area and pore volume, facilitating efficient ion transport and minimizing diffusion resistance. The BET analysis and pore size distribution data indicate that our Zn-Co-P nanowire/Ni foam material has a good nanopore structure, providing a specific surface area and more electrochemical active sites. This structure enhances ion diffusion, electrolyte access, and overall electrochemical performance, making it suitable for applications in supercapacitors and batteries.
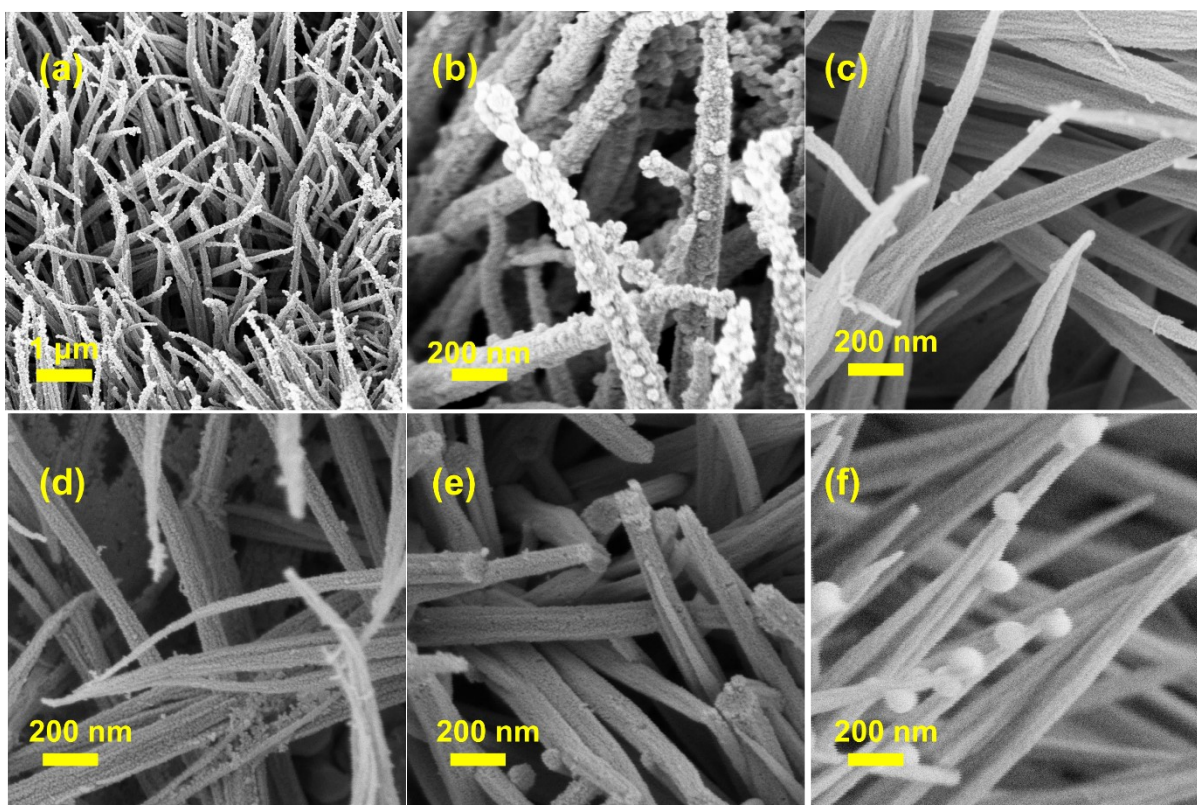
**Fig. S3** FE-SEM image of as-synthesized (a-b) $Ni_{0.5}V_{0.5}$–Se/Zn-Co-P, (c) $Ni_{0.25}V_{0.75}$–Se/Zn-Co-P, (d) $Ni_{0.75}V_{0.25}$–Se/Zn-Co-P, (e) Ni–Se/Zn-Co-P, and (f) V–Se /Zn-Co-P.
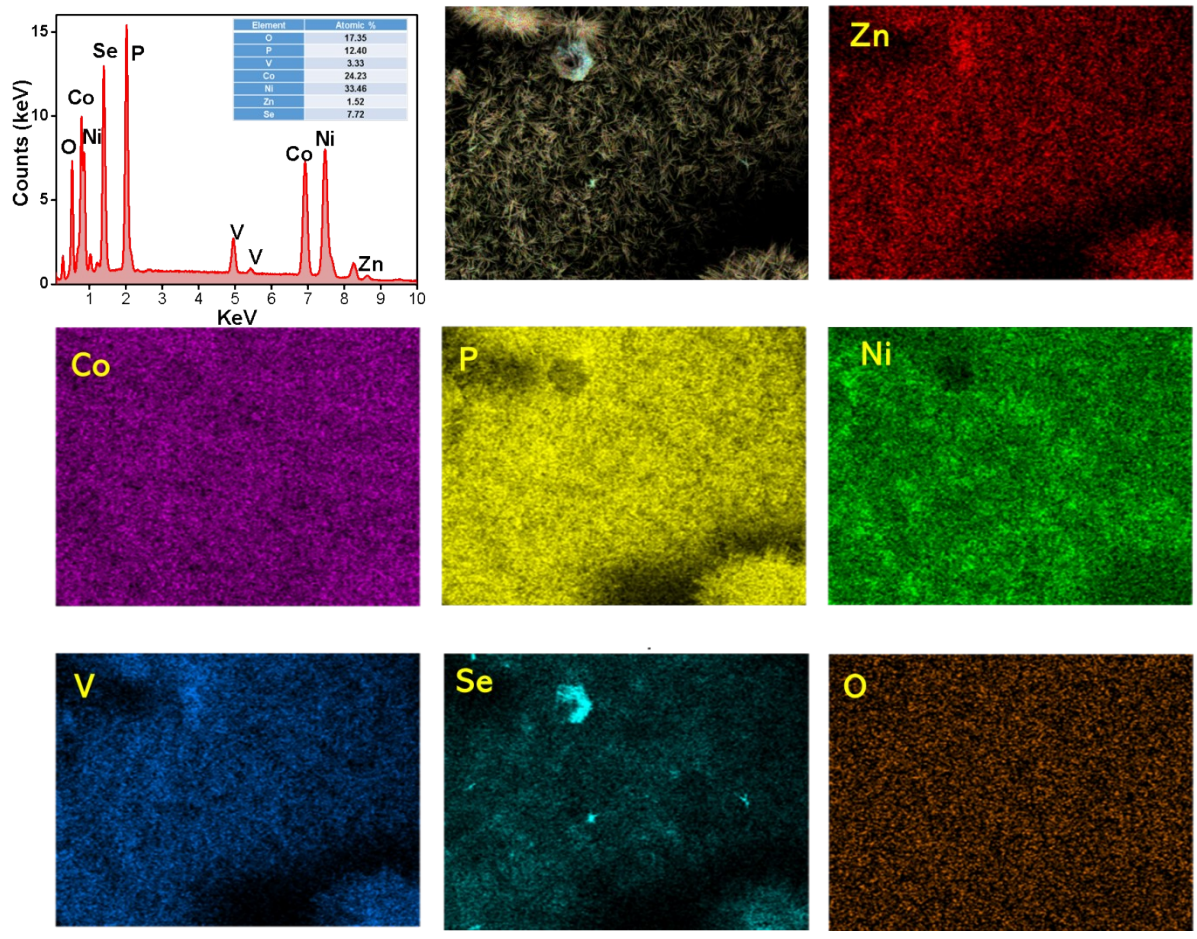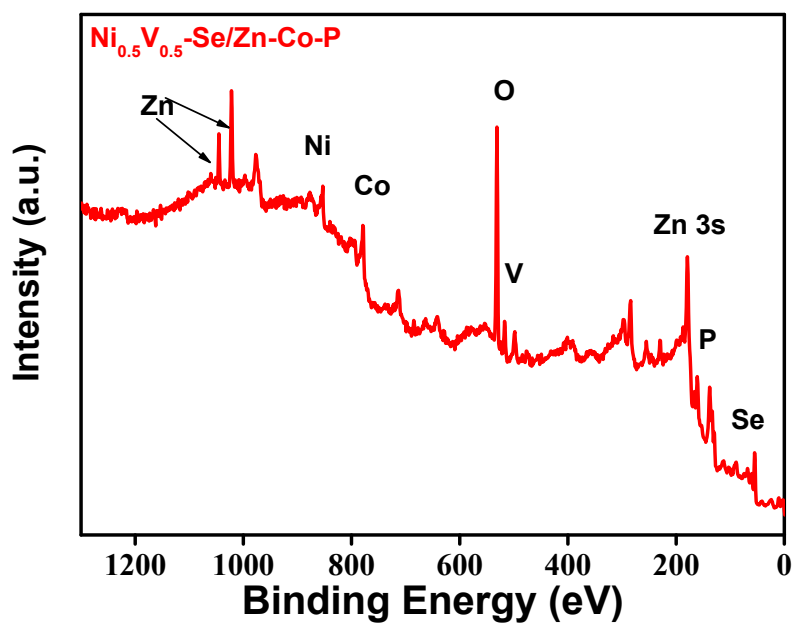
**Fig. S4** The EDX analysis of $Ni_{0.5}V_{0.5}$–Se/Zn-Co-P NWAs

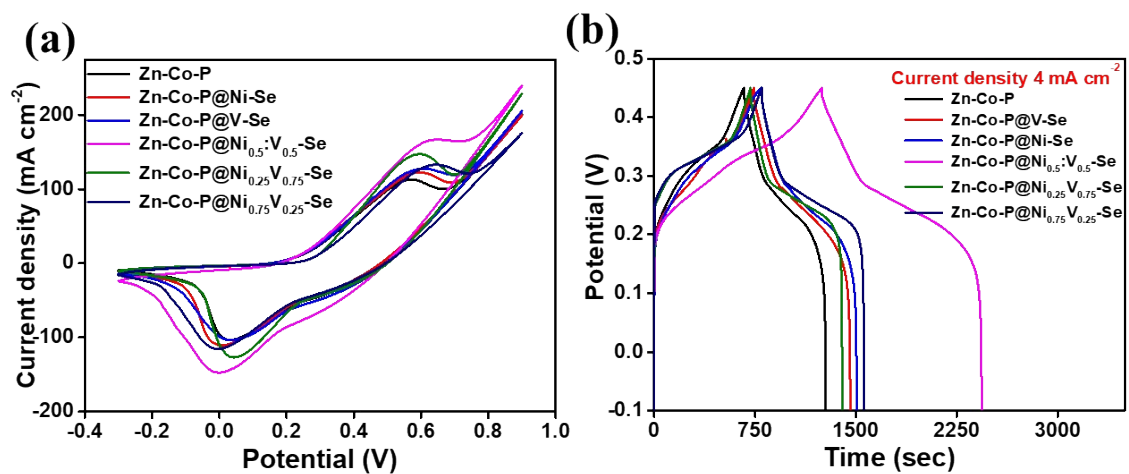**Fig. S5** Full survey XPS spectra of $Ni_{0.5}V_{0.5}$–Se/Zn-Co-P NWAs

**Fig. S6** Electrochemical performance of Zn-Co-P NWs in comparison with different compositions of $Ni_x$:$V_y$–Se/Zn-Co-P electrodes: (a) CV curves measured at the scan rate of 15 mV s$^{-1}$ and (b) GCD curves at 4.0 mA cm$^{-2}$.

**Fig. S7** (a) log (peak current, mA) vs log (scan rate, mV s$^{-1}$) graph of Zn-Co-P. (a) log (peak current, mA) vs log (scan rate, mV s$^{-1}$) graph of Ni-Se/Zn-Co-P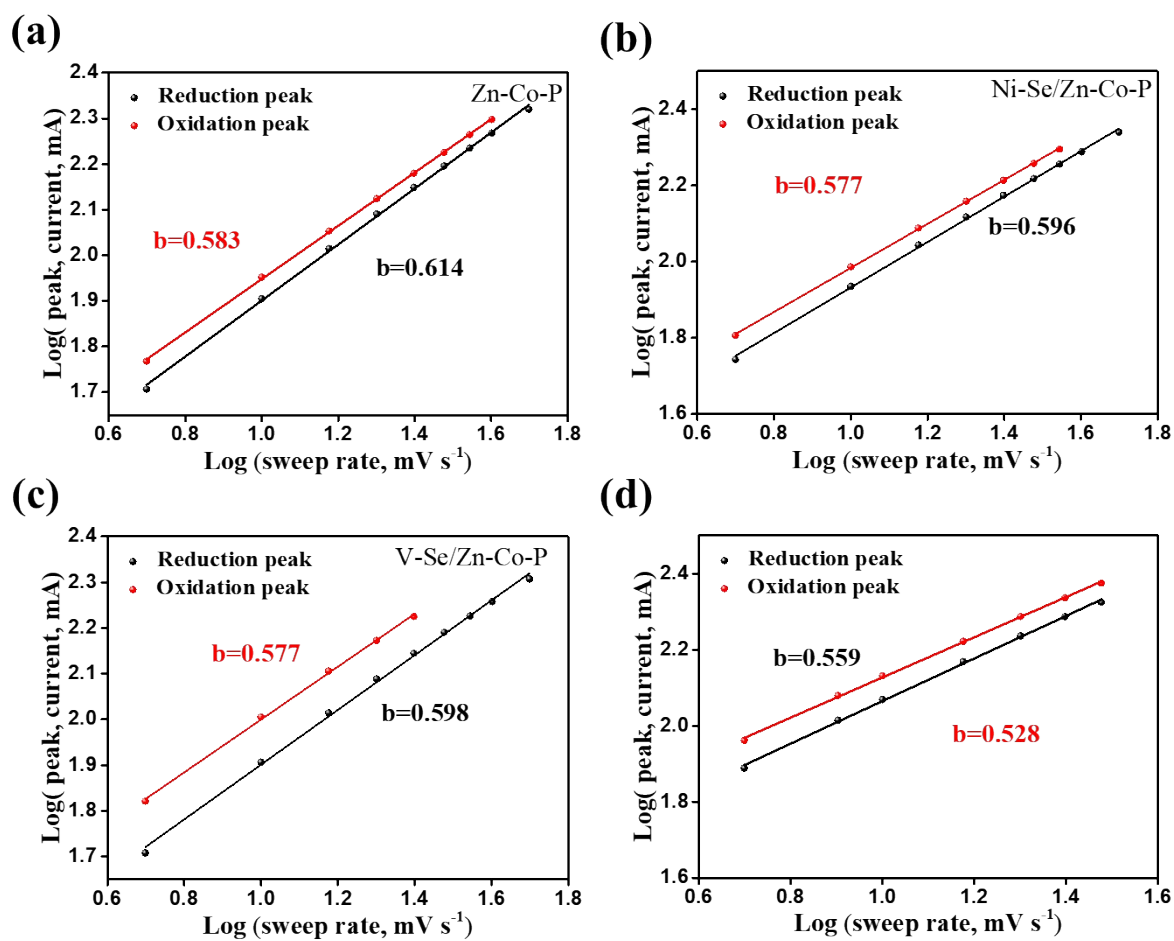. (c) log (peak current, mA) vs log (scan rate, mV s$^{-1}$) graph of V-Se/Zn-Co-P.(d) log (peak current, mA) vs log (scan rate, mV s$^{-1}$) graph of Ni$_{0.5}$V$_{0.5}$–Se/Zn-Co-P
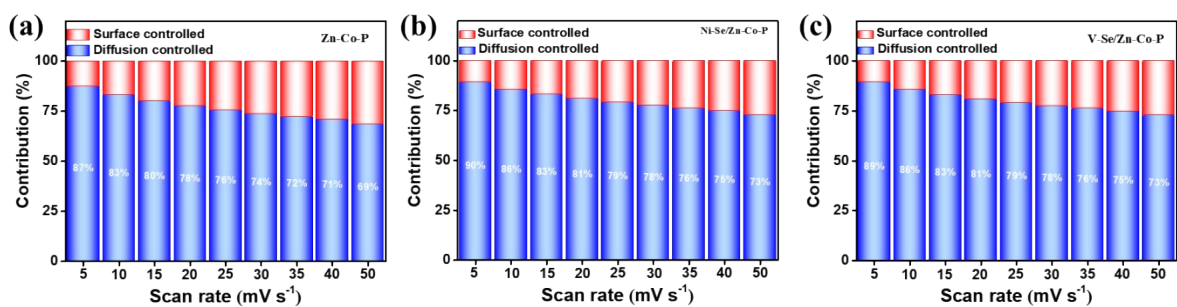
**Fig. S8** (a)The diffusion and surface-controlled capacities contribute of Zn-Co-P at various scan rates. (a)The diffusion and surface-controlled capacities contribute of Ni-Se/Zn-Co-P at various scan rates. (c)The diffusion and surface-controlled capacities contribute of V-Se/Zn-Co-P at various scan rates.
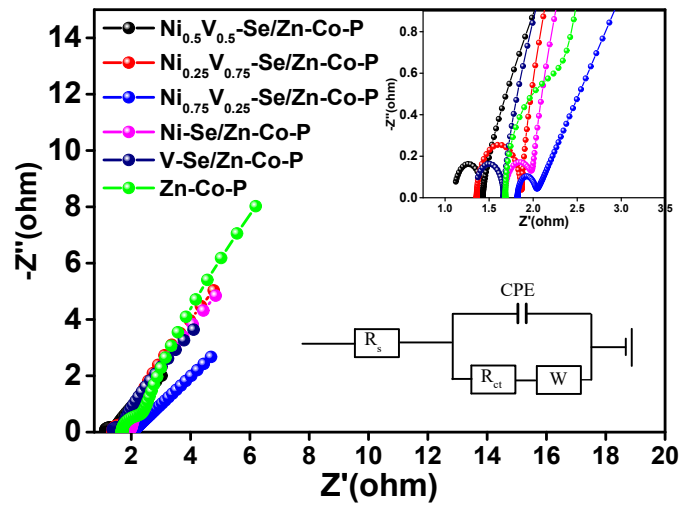
**Fig. S9.** (e) EIS spectra of the different compositions electrodes (inset: high-magnification EIS and equivalent circuit).

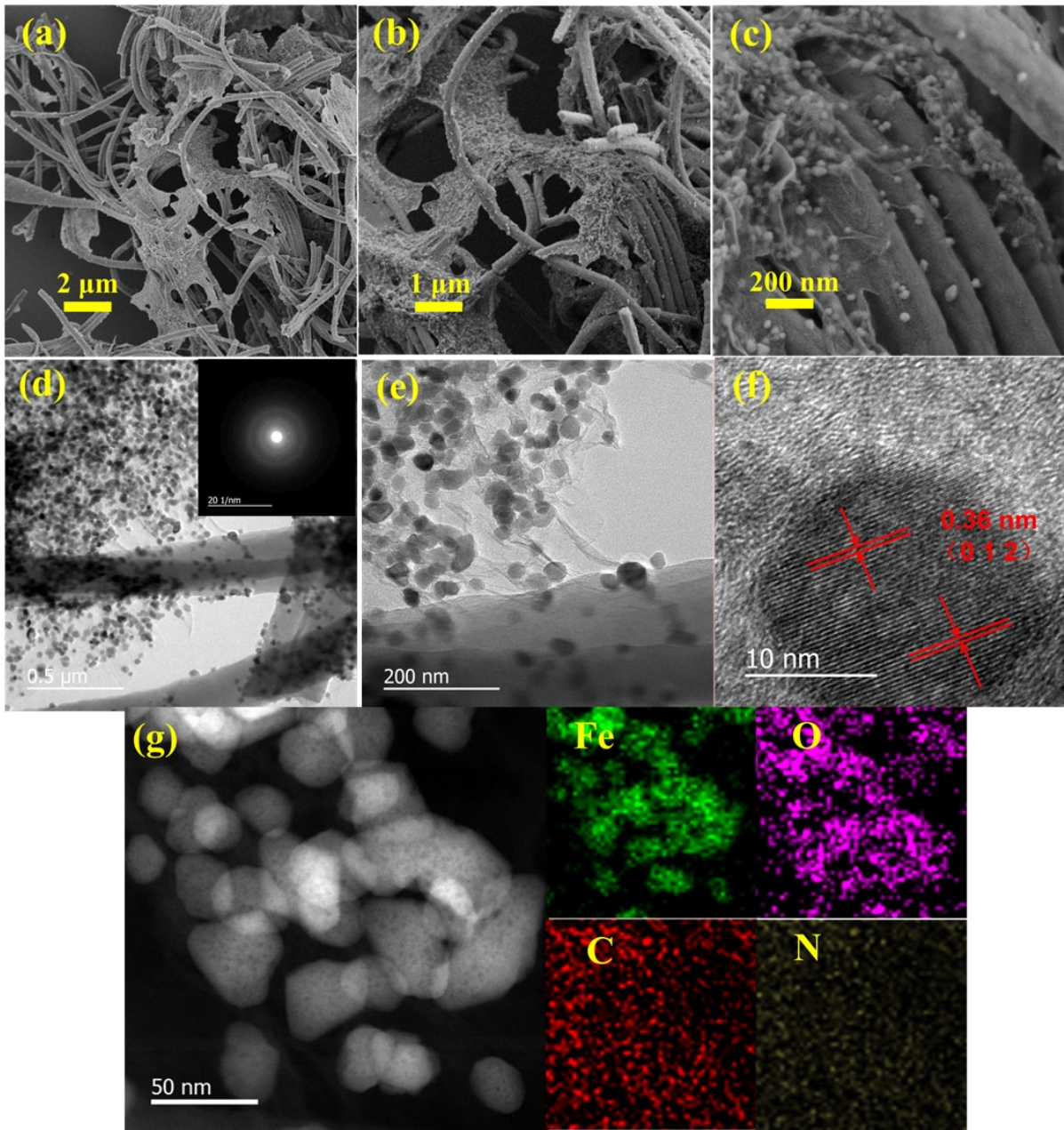**Fig. S10** (a-c) FE–SEM images of as-syntheize Fe$_2$O$_3$@CNFs/N-rGO aerogel. (d-f) Typical TEM and HRTEM images of the hierarchical Fe$_2$O$_3$ @CNFs/N-rGO aerogel. (g) HAADF–STEM–EDX mapping images of the Fe$_2$O$_3$ @CNFs/N-rGO aerogel, demonstrating the homogeneous distribution of Fe, O, C, N elements.

**(a)**

**(b)**
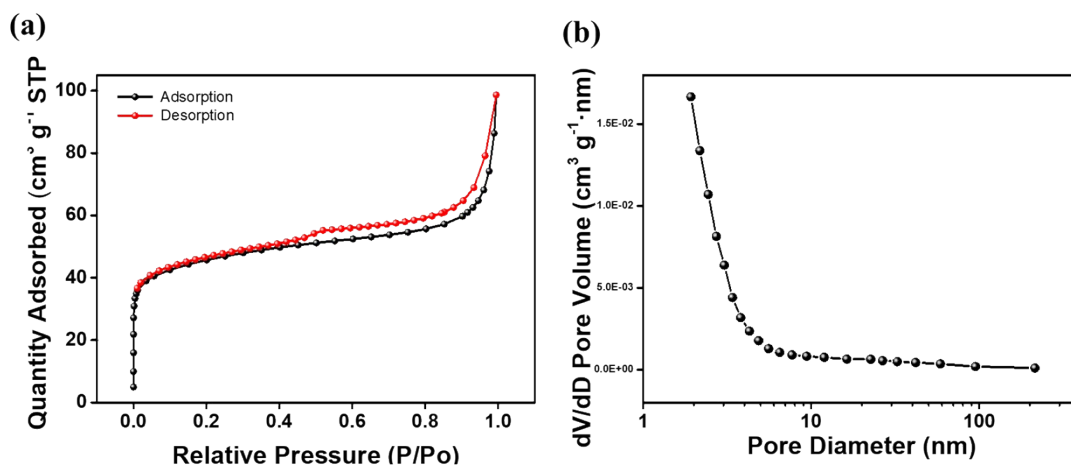
**Fig.S11** (a) and (b) show the adsorption-desorption isotherms and pore size distribution of Fe$_2$O$_3$@CNFs/N-rGO

Figs. S11a,b highlights the adsorption-desorption isotherms and pore size distribution of Fe$_2$O$_3$@CNFs/N-rGO electrode. The BET surface area of 151.2336 m$^2$/g indicates a large surface area available for electrochemical reactions. This high surface area is crucial for enhancing the capacitance and energy storage capability of the electrode. The presence of mesopores and macropores in the material facilitates efficient ion transport and reduces diffusion resistance. This porous structure contributes to the high-rate capability and cycling stability of the electrode.
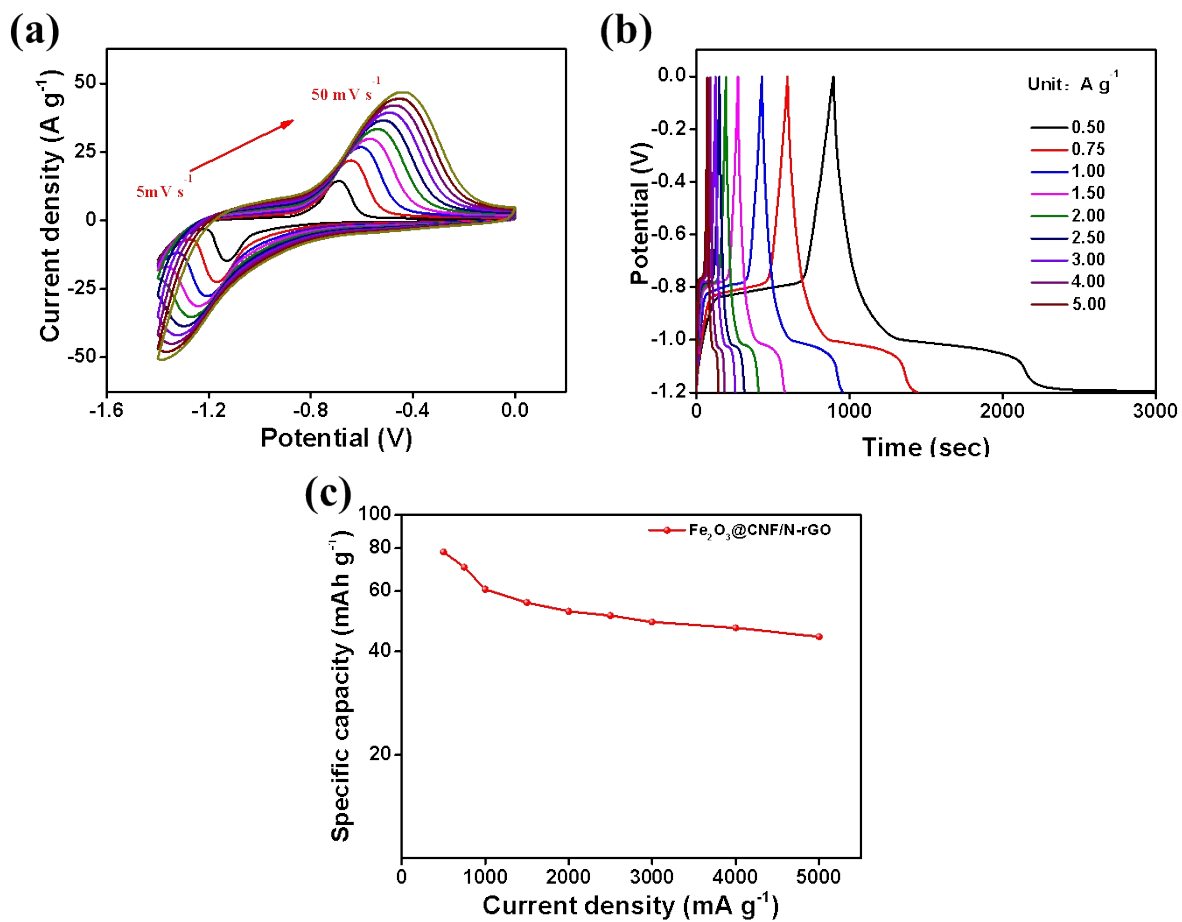
**Fig. S12** (a) CV curves of the $Fe_2O_3$@CNFs/N-rGO at different scan rate. (b) The GCD curves of the $Fe_2O_3$@CNFs/N-rGO at different current density. (c) The specific capacity vs. current density of $Fe_2O_3$@CNFs/N-rGO.
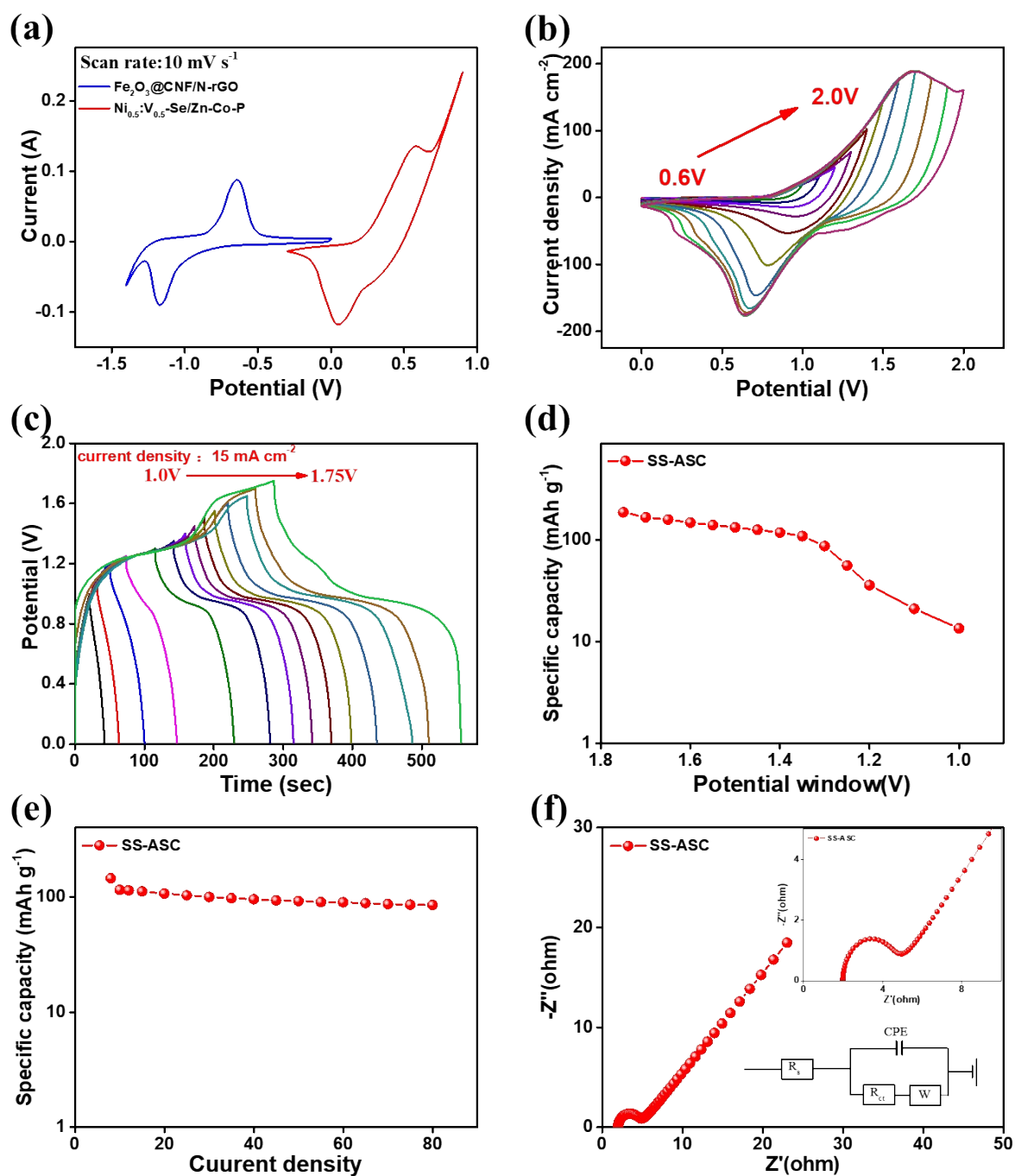
**Fig. S13** (a) CV curves of the $Ni_{0.5}V_{0.5}$-Se/Zn-Co-P and $Fe_2O_3$@CNFs/N-rGO electrodes examined under the three-electrode configuration system. (b) CV curves (scan rate 50 mV s$^{-1}$) of SS-ASC at various operating voltage windows. (c) GCD curves of SS-ASC at various operating voltage windows. (d) The specific capacity vs. operating voltage windows of SS-ASC. (e) The specific capacity vs. current density of SS-ASC (f) The EIS curves of SS-ASC.

**Table.S1** ICP Test Results Analysis Elemental Concentrations and Atomic Percentages of $Ni_x$:$V_y$–Se/Zn–Co–P NWAs electrode

| Element | Average Concentration (ppm) | Atomic Percentage (%) |
|---|---|---|
| Ni | 0.11 | 16.41 |
| Co | 0.108 | 16.05 |
| Zn | 0.103 | 13.8 |
| P | 0.091 | 25.73 |
| Se | 0.093 | 10.31 |
| V | 0.103 | 17.71 |

**Table S2.** Electrode properties comparison with reported literatures.

| Electrode Materials | Areal Capacitance / capacity | Specific capacitance /capacity | Current load | Electrolyte | Stability (Cycles) | Ref. |
|---|---|---|---|---|---|---|
| $CoNi_2S_4$/SNGA | - | 318.3 mAh g$^{-1}$ | 1 A g$^{-1}$ | 6 M KOH | 95.8% (10000) | [7] |
| Ni-Co-S/G | - | 1492 F g$^{-1}$ | 1 A g$^{-1}$ | 6 M KOH | 90% (8000) | [8] |
| VACNTF@MoSe | - | 435 F·g$^{-1}$ | 1 A g$^{-1}$ | 2 M KOH | 92% (5000) | [9] |
| $MoSe_2$/graphene Nanosheet | - | 945 F·g$^{-1}$ | 1 A g$^{-1}$ | 6 M KOH | 92% (2000) | [10] |
| CoSe Nanosheet | - | 70.6 mAh g$^{-1}$ | 1 A g$^{-1}$ | 2M KOH | - | [11] |
| NiSe@$MoSe_2$ Nanosheet | - | 128.2 mAh g$^{-1}$ | 1 A g$^{-1}$ | 2 M KOH | 93.7% (1000) | [12] |
| $CoSe_2$/$Ni_{0.85}$Se Nanotube | - | 171 mAh g$^{-1}$ | 1.9 A g$^{-1}$ | 6 M KOH | 95.3% (6000) | [13] |
| $MoSe_2$-Ni(OH)$_2$ Nanosheet | - | 146.9 mAh g$^{-1}$ | 1 A g$^{-1}$ | 6 M KOH | 90% (3000) | [14] |
| $CoSe_2$/$MoSe_2$ Hollow Nanosphere | - | 211.97 mAh g$^{-1}$ | 1 A g$^{-1}$ | 3 M KOH | 94.2% (2000) | [15] |
| Co-Mo-Se Nanosheet arrays | - | 221.7 mAh g$^{-1}$ | 1 A g$^{-1}$ | 6 M KOH | 95% (8000) | [16] |
| $Ni_3S_2$@PPy | 3148 mF cm$^{-2}$ | - | 2 mA cm$^{-2}$ | 2 M KOH | 91.2% (4000) | [17] |
| Zn–Co–Se | - | 313.45 C g$^{-1}$ | 0.5 A g$^{-1}$ | 1 M KOH | 95% (3000) | [18] |
| Zn-Ni-Al-Co oxide | 3.27 F cm$^{-2}$ | - | 1 A g$^{-1}$ | 2 M KOH | - | [19] |
| FeNiP@CoNi-LDH | - | 2286 F g$^{-1}$ | 1 A g$^{-1}$ | 1 M KOH | 96% (5000) | [20] |
| Zn-Ni-Co-P | - | 2820 F g$^{-1}$ | 3 A g$^{-1}$ | 3 M KOH | - | [21] |
| $Zn_{0.33}Co_{0.67}$P | - | 2115.5 F g$^{-1}$ | 1 A g$^{-1}$ | 6 M KOH | 80.4% (7000) | [22] |
| **$Ni_{0.5}V_{0.5}$-Se/Zn-Co-P NWAs** | **1.73 mAh cm$^{-2}$** | **693.03 mAh g$^{-1}$** | **2 mA cm$^{-2}$** | **2 M KOH** | **96.4% (10000)** | **This work** |

**Table S3**. ASCs device properties comparison with reported literature

| Reported ASC Device | Energy density (Wh kg$^{-1}$) | Power density (W kg$^{-1}$) | Device Window (V) | Electrolyte | Stability (Cycles) | Ref. |
|---|---|---|---|---|---|---|
| NiCo$_2$S$_4$//G/C | 42.3 | 476 | 0-1.6 | 6 M KOH | 78.6% (10000) | [8] |
| ZnNiAlCoO//RGO | 72.4 | 533 | 0-1.5 | 2 M KOH | 90% (10000) | [19] |
| FeCo$_2$S$_4$//3D PNG | 76.1 | 755 | 0-1.6 | KOH/PVA | 82% (10000) | [23] |
| Zn–Co–Se//graphene-ink | 16.97 | 269.81 | 0-1.6 | 1 M KOH | 95% (5000) | [18] |
| CoSe$_2$/MoSe$_2$-3-1//AC | 51.84 | 799.2 | 0-1.6 | 3 M KOH | 93.4% (10000) | [15] |
| MoSe$_2$-Ni(OH)$_2$//AC | 43 | 817 | 0-1.6 | 6 M KOH | 85% (5000) | [13] |
| NCP@P-rGO//AC | 39.7 | 790 | 0-1.6 | 3 M KOH | 90% (5000) | [24] |
| NiSe@MoSe$_2$//N-PMCN | 32.6 | 415 | 0-1.65 | 2M KOH | 91.4% (5000) | [12] |
| CCS@GO//AC | 54.6 | 700 | 0-1.4 | 3M KOH | 82.5% (10000) | [25] |
| Mo-Ni2P/Co2P //AC | 35.56 | 800.0 | 0-1.6 | 3M KOH | 84.83 (15000) | [26] |
| CoCuP@400// O, N, S@AC | 37.3 | 12308.3 | 0-1.6 | 6M KOH | 89% (10000) | [27] |
| CoZnNiP/C-2 // hierarchical porous carbon (HPC) | 45.9 | 533.3 | 0-1.6 | KOH/PVA | 92.2% (8000) | [28] |
| FeNiCoP/rGO // N–C/rGO | 52.9 | 8579.5 | 0-1.5 | 6M KOH | 82.8% 5000 | [29] |
| Co–Mo–Se//AC | 44.7 | 1094 | 0-1.55 | KOH/PVA | 90.7% (8000) | [16] |
| Co/Co2P/CoP//AC | 37.87 | 799.6 | 0-1.6 | 2M KOH | 80% (5000) | [30] |
| MnO$_2$@Co$_9$S$_8$//AC | 35 | 240 | 0-1.6 | 3M KOH | 97.5% (36000) | [31] |
| **Ni$_{0.5}$V$_{0.5}$-Se/Zn-Co-P //Fe$_2$O$_3$@CNFs@ N-rGO** | **123.6** | **1050.2** | **0-1.7** | **PVA/ KOH** | **95.8% (10000)** | **This work** |

**Reference**

[1] T. Kshetri, D.T. Tran, T.I. Singh, N.H. Kim, K.-t. Lau, J.H. Lee, Composites Part B: Engineering, 178 (2019) 107500.

[2] G. Wang, L. Zhang, J. Zhang, Chemical Society Reviews, 41 (2012) 797-828.

[3] J. Liu, J. Wang, C. Xu, H. Jiang, C. Li, L. Zhang, J. Lin, Z.X. Shen, Advanced Science, 5 (2018) 1700322.

[4] Y. Shao, M.F. El-Kady, J. Sun, Y. Li, Q. Zhang, M. Zhu, H. Wang, B. Dunn, R.B. Kaner, Chemical Reviews, 118 (2018) 9233-9280.

[5] Y. Li, R. Li, D. Wang, H. Xu, F. Meng, D. Dong, J. Jiang, J. Zhang, M. An, P. Yang, International Journal of Hydrogen Energy, 46 (2021) 5131-5149.

[6] S.H. Nagarajarao, A. Nandagudi, R. Viswanatha, B.M. Basavaraja, M.S. Santosh, B.M. Praveen, A. Pandith, ChemEngineering, 6 (2022) 5.

[7] G. He, M. Qiao, W. Li, Y. Lu, T. Zhao, R. Zou, B. Li, J.A. Darr, J. Hu, M.-M. Titirici, I.P. Parkin, Advanced Science, 4 (2017) 1600214.

[8] J. Yang, C. Yu, X. Fan, S. Liang, S. Li, H. Huang, Z. Ling, C. Hao, J. Qiu, Energy & Environmental Science, 9 (2016) 1299-1307.

[9] Y. Liu, W. Li, X. Chang, H. Chen, X. Zheng, J. Bai, Z. Ren, Journal of Colloid and Interface Science, 562 (2020) 483-492.

[10] B. Kirubasankar, S. Vijayan, S. Angaiah, Sustainable Energy & Fuels, 3 (2019) 467-477.

[11] Y. Zhu, Z. Huang, Z. Hu, L. Xi, X. Ji, Y. Liu, Electrochimica Acta, 269 (2018) 30-37.

[12] H. Peng, J. Zhou, K. Sun, G. Ma, Z. Zhang, E. Feng, Z. Lei, ACS Sustainable Chemistry & Engineering, 5 (2017) 5951-5963.

[13] J. Lin, H. Wang, Y. Yan, X. Zheng, H. Jia, J. Qi, J. Cao, J. Tu, W. Fei, J. Feng, Journal of Materials Chemistry A, 6 (2018) 19151-19158.

[14] B. Kirubasankar, P. Palanisamy, S. Arunachalam, V. Murugadoss, S. Angaiah, Chemical Engineering Journal, 355 (2019) 881-890.

[15] F. Ma, J. Lu, L. Pu, W. Wang, Y. Dai, Journal of Colloid and Interface Science, 563 (2020) 435-446.

[16] C. Miao, C. Zhou, H.-E. Wang, K. Zhu, K. Ye, Q. Wang, J. Yan, D. Cao, N. Li, G. Wang, Journal of Power Sources, 490 (2021) 229532.

[17] J. Ren, M. Shen, Z. Li, C. Yang, Y. Liang, H.-E. Wang, J. Li, N. Li, D. Qian, Journal of Power Sources, 501 (2021) 230003.

[18] V.T. Chebrolu, B. Balakrishnan, D. Chinnadurai, H.-J. Kim, Advanced Materials Technologies, 5 (2020) 1900873.

[19] Q. Zhang, B. Zhao, J. Wang, C. Qu, H. Sun, K. Zhang, M. Liu, Nano Energy, 28 (2016) 475-485.

[20] L. Wan, D. Chen, J. Liu, Y. Zhang, J. Chen, M. Xie, C. Du, Journal of Power Sources, 465 (2020) 228293.

[21] X. Lei, S. Ge, Y. Tan, Z. Wang, J. Li, X. Li, G. Hu, X. Zhu, M. Huang, Y. Zhu, B. Xiang, ACS Applied Materials & Interfaces, 12 (2020) 9158-9168.

[22] W. Chu, Y. Hou, J. Liu, X. Bai, Y.f. Gao, Z. Cao, Electrochimica Acta, 364 (2020) 137063.

[23] S. Tang, B. Zhu, X. Shi, J. Wu, X. Meng, Advanced Energy Materials, 7 (2017).

[24] U. Javed, G. Dhakal, A.M. Rabie, S. Iqbal, Y.R. Lee, J. Lee, J.J. Shim, Materials Today Nano, 18 (2022) 100195.

[25] K. Karuppasamy, D. Vikraman, S. Hussain, G. Kumar Veerasubramani, P. Santhoshkumar, S.-H. Lee, R. Bose, A. Kathalingam, H.-S. Kim, Chemical Engineering Journal, 427 (2022) 131535.

[26] Y. Dong, X. Yue, J. Gong, Y. Gao, Q. Zheng, K.H. Lam, D. Lin, Journal of Alloys and Compounds, 952 (2023)

169985.

[27] A.M. Kale, R. Velayutham, A.D. Savariraj, M. Demir, B.C. Kim, Materials Today Sustainability, 21 (2023) 100335.

[28] H. Zhang, Y. Wang, C. Chen, X. Wu, Journal of Energy Storage, 55 (2022) 105623.

[29] C. Du, S. Shi, G. Chen, Y. Zhang, Q. Wei, L. Li, G. Wan, Z. Deng, Y. Wu, Y. Su, L. Li, G. Wang, Materials Today Energy, 34 (2023) 101287.

[30] S.-B. Guo, W.-B. Zhang, Z.-Q. Yang, S.-S. Chai, X.-L. Zhang, X. Zhou, X.-W. Han, J. Long, Journal of Alloys and Compounds, 944 (2023) 169160.

[31] Q. Hu, X. Jiang, M. He, Q. Zheng, K.H. Lam, D. Lin, Electrochimica Acta, 338 (2020) 135896.